Hydrodynamic Characterization of Surfactant Encapsulated Carbon Nanotubes Using an Analytical Ultracentrifuge

Michael S. Arnold,[†,¶] Jin Suntivich,[†,¶] Samuel I. Stupp,[†,‡,§,⊥] and Mark C. Hersam[†,‡,⊥,*]

[†]Department of Materials Science and Engineering, Northwestern University, Evanston, Illinois 60208-3108, [‡]Department of Chemistry, Northwestern University, Evanston, Illinois 60208-3113, [§]Feinberg School of Medicine, and [⊥]Insitute for BioNanotechnology in Medicine, Northwestern University, Chicago, Illinois 60611-3008. [¶]These authors contributed equally to this work.

ABSTRACT The hydrodynamic properties of surfactant encapsulated single-walled carbon nanotubes (SWNTs) have been characterized by optically measuring their spatial and temporal redistribution *in situ* in an analytical ultracentrifuge. The measured redistribution profiles are fit to the Lamm equation, thus determining the sedimentation, diffusion, and hydrodynamic frictional coefficients of the surfactant encapsulated SWNTs. For sodium cholate encapsulated SWNTs, we demonstrate that the technique of analytical ultracentrifugation can be utilized to determine the linear packing density of surfactant molecules along the length of the SWNTs, 3.6 ± 0.8 nm^{-1}, and the anhydrous molar volume of the surfactant molecules on the SWNT surfaces, 270 ± 20 $cm^3\ mol^{-1}$. Additionally, analytical ultracentrifugation is used to measure and compare the sedimentation rates of bundled and isolated carbon nanotubes. This study should serve as a guide for designing centrifuge-based processing procedures for preparing samples of SWNTs for a wide variety of applications and studies. Additionally, the results obtained here should aid in understanding the hydrodynamic properties of SWNTs and the interactions between SWNTs and surfactants in aqueous solution.

KEYWORDS: hydrodynamic · surfactant encapsulated · ultracentrifuge · carbon nanotubes · sedimentation · diffusion · density

The preparative ultracentrifuge has proven to be an essential tool for the processing of carbon nanotubes.[1−18] As-grown carbon nanotubes are typically highly aggregated, heterogeneous mixtures of nanostructures that significantly differ in their physical and electronic properties.[1,12,19,20] As-grown carbon nanotubes must first be isolated and then sorted by their physical and electronic properties before they can be utilized in large-scale applications such as integrated circuits, near-infrared emitters and photodetectors, or biochemical sensors.[19] O'Connell *et al.* were the first to demonstrate that isolated and aggregated single-walled carbon nanotubes (SWNTs) could be separated in an ultracentrifuge by exploiting differences in the rate of their centrifugal sedimentation.[12] This seminal work led to discoveries such as near-infrared photoluminescence[12] and permitted fundamental studies of SWNT photophysics.[9,21]

The work of O'Connell *et al.* was recently extended to include separation of SWNTs by diameter, band gap, and electronic type (*e.g.*, metallic *versus* semiconducting) using the technique of density gradient ultracentrifugation (DGU).[1,2,6,22,23] Semiconducting SWNTs produced by DGU are useful for transistor logic, amplification, and sensing,[1] whereas metallic SWNTs isolated by DGU are better suited as the interconnecting leads of integrated circuits or as the conductive elements of transparent conductors.[1,24,25] Nearly monodisperse SWNTs sorted by their diameter and band gap *via* DGU have also enabled more detailed fundamental studies of SWNT photophysics by reducing spectral overlap.[4,5,8,26−28] Additional ultracentrifuge-based separation techniques have recently been utilized to remove carbonaceous impurities and catalysts from SWNT dispersions,[16] to separate SWNTs by the chemical functionalization on their surfaces,[3,29] and for concentration purposes.[2]

The use of preparative ultracentrifuges to process and sort SWNTs has clearly led to important discoveries and advances in the application and science of SWNTs. Yet, despite these successes, relatively few quantitative studies have been undertaken to understand the hydrodynamics of SWNTs. The most thorough study to date was performed by Nair *et al.* where the hydrodynamic properties of surfactant encapsulated SWNTs were deduced from the buoyant density and spatial spreading of

See the accompanying Perspective by Martel *et al.* on p 2195.

*Address correspondence to m-hersam@northwestern.edu.

Received for review August 12, 2008 and accepted September 19, 2008.

Published online October 3, 2008. 10.1021/nn800512t CCC: $40.75

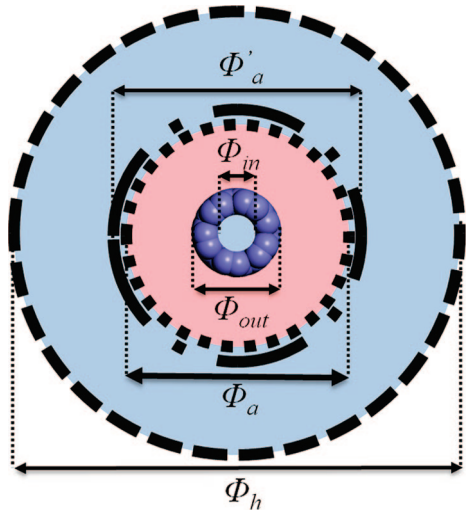

Figure 1. Schematic depicting the SWNT, surfactant, and hydration layers: Φ_{in}, Φ_{out}, Φ_a, Φ'_a, and Φ_h denote the inner and outer diameters of the SWNT and the anhydrous, hydrodynamic, and buoyancy-hydrated diameters of the SWNT−surfactant complex, respectively.

SWNTs at their isopycnic banding positions in density gradients.[11] However, the findings of Nair *et al.* are convoluted by the fact that a large hydration shell (Figure 1) reduces the buoyant density of surfactant−SWNT complexes in aqueous solution. As a result, it is difficult to differentiate the mass and volume of the surfactant layers from the mass and volume of the hydration layers in DGU experiments.

An alternative method for characterizing the hydrodynamic properties of surfactant encapsulated SWNTs is analytical ultracentrifugation. By measuring the *transient* spatial and temporal distribution of SWNTs in water *in situ* in a centrifugal force field (Figure 2), the sedimentation, diffusion, and hydrodynamic frictional coefficients of surfactant−SWNT complexes can be directly determined. Analytical ultracentrifugation is a more direct means of study because the hydration layer surrounding surfactant−SWNT complexes (Figure 1) is "transparent" in water due to the fact that the density of the hydration layer is nearly identical to the density of bulk water.[30−32] Consequently, the sedimentation velocity of a surfactant−SWNT complex in water depends

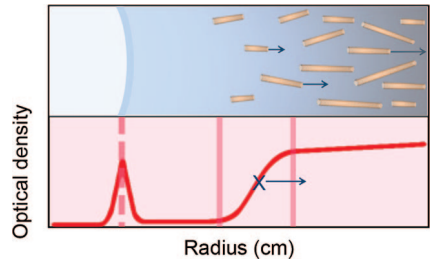

Figure 2. Schematic of SWNTs in an analytical ultracentrifuge cell (top) and a corresponding plot of optical density *versus* radius (bottom). The meniscus of the solution is identified by an artificial peak in the optical density (dashed line), and the sedimenting boundary is found between the vertical, solid red lines, marked by the symbol X.

only on the anhydrous partial specific volume of the surfactant−SWNT complex and not the hydrated partial specific volume, which is measured *via* DGU. Therefore, a more sensitive measure of the anhydrous properties of surfactant encapsulated SWNTs can be obtained using analytical ultracentrifugation.

In the first part of this study, a sample of sodium cholate encapsulated SWNTs sorted by DGU that are nearly monodisperse in diameter is characterized. The narrow diameter distribution of SWNTs and the lack of bundles or aggregates in this sample make it ideal for characterizing the sedimentation and diffusion of surfactant encapsulated SWNTs and for developing a relevant model for SWNT sedimentation. Furthermore, sodium cholate is an appropriate surfactant for this study because it lends itself well to enabling high quality separation of SWNTs *via* DGU. In the second part of this study, the anhydrous partial specific volume and anhydrous density of sodium cholate encapsulated SWNTs are determined by comparing their sedimentation coefficients in H_2O and D_2O. These measurements allow the linear packing density of sodium cholate molecules, the anhydrous molar volume of sodium cholate molecules on the surfaces of the SWNTs, and the average SWNT length to be deduced. Then, the effects of SWNT aggregation on sedimentation coefficient are examined. Finally, in the Supporting Information, a series of predictions for how the sedimentation coefficient and buoyant density of a SWNT−surfactant complex should vary as a function of nanotube diameter and length, the linear density of adsorbed surfactant, and the hydration thickness are developed.

RESULTS AND DISCUSSION

Theory. The motion of a SWNT in aqueous solution in a centrifuge is driven by two processes: diffusion due to Brownian motion and sedimentation in response to the centrifugal force. In general, the sedimentation and diffusion coefficients of a particle are determined by the molar mass of the particle, M, its anhydrous partial specific volume, υ, and its Stokes hydrodynamic frictional drag coefficient, f.[33] The sedimentation velocity, u, in response to the centrifugal force, $\omega^2 r$, is described by

$$u = \omega^2 r \times s \tag{1}$$

where ω is the angular velocity and r is the distance from the SWNT to the center of the rotor. In general, s is given by the Svedberg relation

$$s = \frac{M(1 - \rho_s \upsilon)}{N_A f} \tag{2}$$

where ρ_s is the density of the solvent and N_A is Avogadro's constant. The diffusion coefficient, D, of a particle can also be expressed as a function of the

Stokes hydrodynamic friction drag coefficient according to the Stokes−Einstein relation

$$D = \frac{k_B T}{f} \quad (3)$$

where k_B is the Boltzmann constant and T is temperature.

The Stokes hydrodynamic frictional drag coefficient, f, is a function of the viscosity of the solvent and the size and shape of the hydrated solute particle and is equal to the ratio of the frictional drag force to the sedimentation velocity. For a spherical object, $f = 3\pi\eta d$, where η is the solvent viscosity and d is the diameter of the sphere. For a rigid, one-dimensional rod (length $\ll$ persistence length), the rotationally averaged Stokes hydrodynamic frictional drag coefficient has been determined by Broersma *et al.*[34−37] The expression for f is analogous to the case of a sphere except that the diameter term, d, is replaced by the length of the rod, L, divided by a new term, F, which is dependent on the aspect ratio of the rod-like particle. Specifically, $f = 3\pi\eta L/F(\Phi_h,L)$, where Φ_h is the hydrodynamic diameter of the one-dimensional rod, and L is its length. The SWNTs used in this study are predominantly in the range of 100−500 nm in length,[2] less than the experimentally measured persistence length of SWNTs in solution which is greater than 1000 nm,[38−40] thus the Broersma model for rigid rods applies. Often, it is simpler to express the hydrodynamic frictional coefficient of a particle as a ratio of the actual hydrodynamic frictional coefficient of the particle to the hypothetical hydrodynamic frictional coefficient that the particle would have if it were reshaped into a sphere of equal mass and volume. For SWNTs of hydrodynamic diameter 10−30 Å and L = 500−5000 Å, the calculated ratio of the actual frictional coefficient to the frictional coefficient of an equivalent sphere ranges between 2 and 9.

When a monodisperse population of particles is present, the particles' temporal and spatial distribution in a sector-shaped centrifugation cell, considering both sedimentation and diffusion, is governed by the single component Lamm equation

$$\frac{\partial c(r,t)}{\partial t} = \frac{1}{r}\frac{\partial}{\partial r}\left(rD\frac{\partial c(r,t)}{\partial r} - s\omega^2 r^2 c(r,t)\right) \quad (4)$$

where c is concentration, r is radius, t is time, D is the diffusion coefficient, and s is the sedimentation coefficient.[33,41] When multiple species are present, the net concentration profile, $c(r,t)$, can be modeled by a superposition of solutions to the single component Lamm equation such that

$$c(r,t) = \sum_{i=1}^{n} \alpha_i c_i(r,t) \quad (5)$$

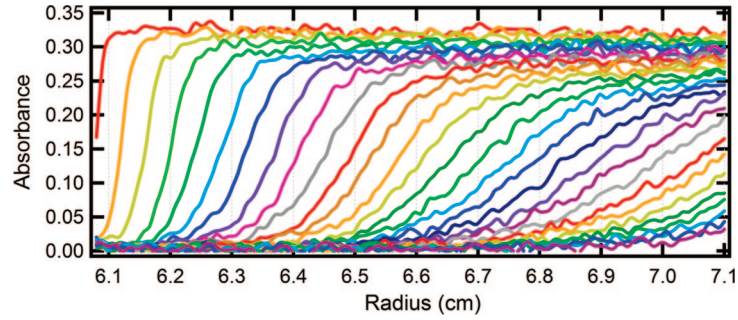

Figure 3. Experimental $c(r,t)$ data for sodium cholate encapsulated SWNTs.

where the sum is over n different sedimenting species and α_i is related to the initial concentration of each species. It should be noted that there can be distinct s_i and D_i for each species, and each $c_i(r,t)$ is determined by the single component Lamm equation (eq 4). For the case of SWNTs, a continuous distribution of species is expected corresponding to SWNTs of various lengths. Therefore, s_i and D_i and the shape of $c_i(r,t)$ will vary as a function of the SWNT length.

Fitting to Models Based on the Lamm Equation. A sample of sodium cholate encapsulated SWNTs that had been sorted by diameter *via* DGU and enriched in the (6,5) chirality of SWNTs was initially studied. Typical yields for the DGU process are 5−10%.[1] This monodisperse sample was utilized to minimize complications arising from variations in SWNT diameter and to ensure that the SWNT population consisted of predominantly isolated, unbundled SWNTs. Experimentally measured $c(r,t)$ data optically collected using the analytical ultracentrifuge are depicted in Figure 3 for this sample with H_2O as the solvent. Initially, at $t = 0$, prior to ultracentrifugation, the optical density of the SWNT solution, and thus the concentration, was homogeneous and uniform. However, for $t > 0$, net sedimentation of the SWNTs occurred in the direction of the centrifugal force, from smaller to larger radii. Gradually, the top of the cell became depleted of SWNTs and a boundary between the SWNT-depleted region and the SWNT-rich region developed. With increasing time, this boundary broadened and moved in the direction of the centrifugal force until all of the SWNTs had sedimented to the bottom of the cell. The spatial broadening of the boundary layer with increasing time is attributed to both diffusion and molecular weight (*i.e.*, length) polydispersity.

To gain more information about the hydrodynamic properties of the SWNTs in this sample, the measured $c(r,t)$ data set was fit to the multicomponent Lamm equation (eq 5) using the software package SEDFIT.[33,41] The value of s_i was fixed to a range of values spanning from 0.1 to 200 Sv on a logarithmic scale (1 Sv = 10^{-13} s), and α_i values were free variables determined by the fit. The best fit and the residuals of the fit are depicted in Figure 4A, and the resulting distribution of α_i *versus* s_i is plotted in Figure 5. In Figure 5, an unregularized α_i

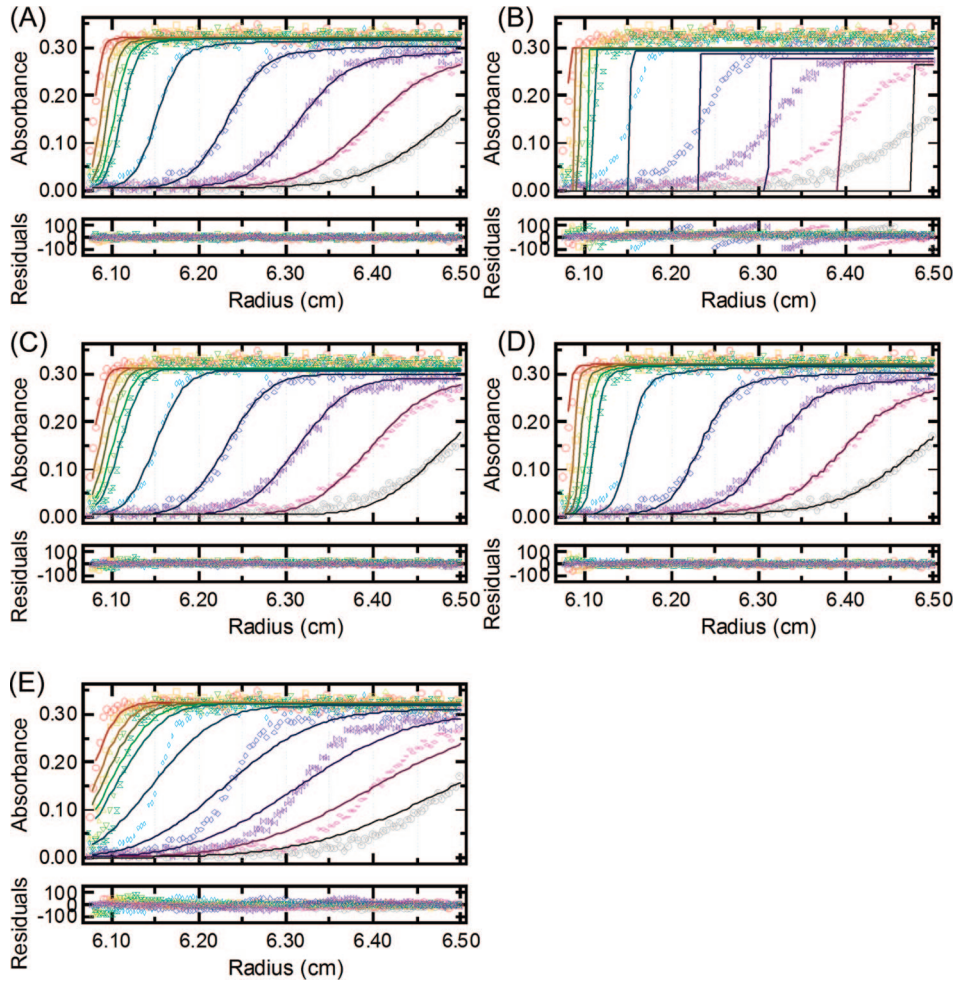

Figure 4. Fitting of the *c*(*r*,*t*) data set for sodium cholate encapsulated SWNTs to various versions of the Lamm equation. The experimental data and fits are denoted by symbols and solid lines, respectively. (A) Best fit using the multicomponent Lamm equation (eq 5) without restrictions on diffusion. (B) Fit of single component Lamm equation (eq 4), ignoring diffusion. (C) Fit of single component Lamm equation (eq 4), considering diffusion. (D) Fit of multicomponent Lamm equation (eq 5), ignoring diffusion. (E) Fit of multicomponent Lamm equation (eq 5), with assumption of spherical particles such that $f_{SWNT}/f_{sphere} = 1$. The root-mean-square deviation for each fit is 8.94, 36.3, 14.1, 9.27, and 15.1, respectively. Residual scale is 1/1000 of the absorbance scale.

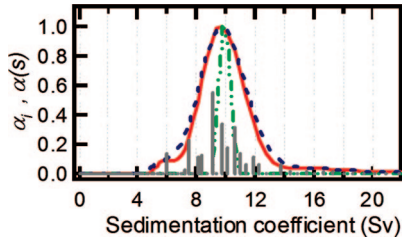

Figure 5. The α_i and $\alpha(s)$ distributions for sodium cholate encapsulated SWNTs. The gray vertical bars represent the unregularized α_i distribution resulting from the fitting of the experimentally measured *c*(*r*,*t*) data to the multicomponent Lamm equation (eq 5) without restrictions on diffusion (see Figure 4A). The solid red curve is the corresponding continuous regularized $\alpha(s)$. The blue dashed curve is the continuous regularized $\alpha(s)$ resulting from the fitting of the experimentally measured *c*(*r*,*t*) to the multicomponent Lamm equation (eq 5) ignoring diffusion (see Figure 4D). The green double-dot dashed curve is the continuous regularized $\alpha(s)$ resulting from the fitting of the experimentally measured *c*(*r*,*t*) to the multicomponent Lamm equation (eq 5) with $f_{SWNT}/f_{sphere} = 1$ (see Figure 4E).

distribution is plotted as discrete vertical bars and an equivalent, regularized distribution is plotted as a solid, continuous curve. The continuous distribution, specified as $\alpha(s)$, is more physically realistic and is mathematically derived from the unregularized α_i distribution under second-derivative regularization.[33,41] Both distributions produce equivalent *c*(*r*,*t*) data sets to within 97% statistical certainty. The regularized $\alpha(s)$ distribution is maximized at 9.9 $\pm$ 0.1 Sv and $D = 7 \pm 2$ $\mu m^2/s$. The ratio of the actual frictional coefficient to the frictional coefficient of an equivalent sphere is 5.3 $\pm$ 1.7 at the maximum of the distribution. The diffusion coefficient measured by analytical ultracentrifugation in this study compares well with the previously measured diffusion coefficient of 4 $\mu m^2/s$ for well isolated HiPCO-grown SWNTs encapsulated by sodium dodecyl benzene sulfonate[42] but is an order of magnitude larger than the diffusion coefficient of 0.4 $\mu m^2/s$ measured for arc-discharge SWNTs dispersed by biopolymers.[43] For the case of the biopolymer dispersed SWNTs, uniform encapsulation of the SWNT with the biopolymer was not observed. Instead, the biopolymer formed large 100 nm spherical particles on the surface of the SWNTs and thus is not directly comparable.

To explore the validity of the fit to the multicomponent Lamm equation (eq 5), several models with other fitting parameters were investigated (Figure 4B−E). First, the single component Lamm equation (eq 4) was explored. In Figure 4B, the solution to the single component Lamm equation with sedimentation as the dominant mass transfer mechanism ($D = 0$) has been fit to the measured *c*(*r*,*t*) data set. According to this model, $s = 9.9$ Sv yields the best fit, which matches the peak sedimentation coefficient determined by the multicomponent Lamm equation (eq 5). However, without broadening of the sedimenting boundary due to polydispersity in *s* or the effects of diffusion, the sedimenting boundary takes the shape of a step function, which does not match the experimental data. By appropri-

ately considering diffusion ($D = 6\ \mu m^2/s$), a much better fit can be obtained due to the broadening of the sedimenting boundary layer, as seen in Figure 4C. However, this fit is inaccurate at long times, and the poor fitting of the experimental data justifies the need to fit to a distribution of multiple species rather than a monodisperse population. Intuitively, it is expected that the length of the SWNTs will be polydisperse, thus further justifying the need to fit the experimental data to the multicomponent Lamm equation (eq 5).

Next, the multicomponent Lamm equation (eq 5) was explored at two extremes: without diffusion and with more rapid diffusion by assuming spherically shaped particles. The rationale for studying the multicomponent solution in the limit of no diffusion is to determine whether a range of species with varying sedimentation coefficients without diffusion is sufficient to describe the data sets. In Figure 4D, the best fit of the multicomponent Lamm equation ignoring diffusion ($D = 0$) is depicted. The resulting regularized $\alpha(s)$ distribution of this fit is plotted as a function of s in Figure 5 as a dashed line. The fit matches the experimental $c(r,t)$ data for most radii and time except at the sedimenting boundary near $t = 0$. The inaccuracy of the fit at this limit is informative and thus further explored. Because the broadening of the boundary layer can be due to either polydispersity or diffusion, it is important to examine the temporal dependencies of each mechanism. If one considers a continuous distribution of sedimenting species, $\alpha(s)$, which is described by a Gaussian distribution with a full width at half-maximum (fwhm) of Δs, then the width of the boundary layer will grow with time, t, as $\Delta s t^1$. On the other hand, the width of the boundary layer resulting from diffusive broadening will go as $(Dt)^{0.5}$, where D is the diffusion constant of the sedimenting species. Thus, for sufficiently long times, the broadening of the boundary layer will be dominated by $\Delta s t^1$. This reasoning explains why the diffusive single-species model is inaccurate at long times in Figure 4C, but the multicomponent model without diffusion remains accurate at long times in Figure 4D. At short times, the width of the boundary layer will be more sensitive to diffusion and cannot be modeled if $D = 0$.

Finally, in Figure 4E, the $c(r,t)$ data set is fit to the multicomponent Lamm equation with the frictional ratio (ratio of the actual frictional coefficient to the frictional coefficient of an equivalent sphere) forced to be 1. In other words, spherical particles were assumed. A result of assuming spherical sedimenting species is a smaller hydrodynamic frictional ratio and a larger diffusion coefficient. The resulting $\alpha(s)$ distribution is plotted as a function of s in Figure 5 as a dotted and dashed curve. The inaccuracy of the fit results from excessive boundary spreading. Therefore, it is apparent that fitting $c(r,t)$ to the multicomponent Lamm equation (eq 5) can sensitively determine both s_i and D_i.

Physical Structure of Sodium Cholate—SWNT Complexes. In the previous section, the analytical ultracentrifuge was utilized to determine the sedimentation and diffusion coefficients of sodium cholate encapsulated SWNTs. These coefficients are intimately related to the structure of the SWNT—surfactant complexes and enable the determination of physical parameters that describe the complexes such as molecular weight, length, surfactant packing density, and the molar volume of surfactant on the SWNT surfaces. In order to extract this information from the sedimentation and diffusion coefficients, the anhydrous partial specific volume of the complexes, υ, must also be known; υ can be determined by comparing the sedimentation rate of the SWNT—surfactant complexes in a H_2O surfactant solution with their sedimentation rate in a D_2O surfactant solution. The technique of comparing sedimentation rates in D_2O and H_2O is commonly used to determine the anhydrous partial specific volume of biomolecules such as proteins.[44] Assuming equivalent surfactant adsorption in water and deuterated water, the ratio of sedimentation coefficients can be expressed as

$$\frac{s_D}{s_H} = \frac{\eta_H(1 - \rho_D\upsilon)}{\eta_D(1 - \rho_H\upsilon)} \quad (6)$$

where "D" subscripts denote in D_2O and "H" subscripts denote in H_2O. The assumption of equivalent surfactant adsorption in water and deuterated water is valid because of the nature of the assembly of the surfactant on the SWNT surfaces, which is driven by hydrophobic collapse. The H_2O $c(r,t)$ and D_2O $c(r,t)$ data sets for sodium cholate encapsulated SWNTs were fit to the multicomponent Lamm equation. The peak, fit sedimentation coefficients in H_2O and D_2O were 9.9 ± 0.1 and 6.9 ± 0.1 Sv, respectively. Accordingly, the anhydrous partial specific volume of the sodium cholate encapsulated SWNTs is $0.53 \pm 0.03\ cm^3\ g^{-1}$. This volume is considerably smaller than the hydrated partial specific volume of $0.93 \pm 0.02\ cm^3\ g^{-1}$ that has been measured by DGU,[1] as expected due to the unimportance of hydration in the anhydrous measurement. The large difference in the partial specific volumes also highlights the significance of the hydration layer in reducing the buoyant density of SWNTs in DGU.

With knowledge of υ, a complete picture of the SWNT—sodium cholate complexes can be deduced. Initially, the "mode" parameters of the SWNT—surfactant complexes are analyzed corresponding to SWNTs at the maximum of the α_i or $\alpha(s)$ distributions. This simplification avoids complications arising from polydispersity in length in the following discussions. The mode hydrodynamic frictional coefficient, f, can be determined from the mode value of D from eq 3, and subsequently the mode molecular weight can be extracted from eq 2. Furthermore, the mode length of the SWNTs, L, the linear density of adsorbed sodium cholate along the

length of the SWNTs, X, and the anhydrous partial molar volume of sodium cholate on the SWNT surface, V', can be quantified.

To extract these latter parameters, a model of the cross section of the SWNT, the surfactant, and the hydration is constructed (Figure 1). The outer and inner diameters of the SWNT, Φ_{out} and Φ_{in}, are defined as Φ_{NT} + 0.34 nm and Φ_{NT} − 0.34 nm, respectively, where Φ_{NT} is the carbon nucleus−carbon nucleus diameter of the SWNT and 0.34 nm is the van der Waals diameter of carbon. For (6,5) SWNTs with a C−C bond distance of 0.142 nm, Φ_{NT} = 0.75 nm. The inner core of a SWNT is expected to be hydrated.[7] In this study, an inner core that is devoid of surfactant molecules with a hydration density of 1.0 g cm^{-3} is assumed.

In the cross-sectional model (Figure 1), surfactant is adsorbed on the exterior surface of the SWNT. When calculating the mass, volume, packing density, and molar volume of these surfactant molecules, no assumptions are made regarding the uniformity of these adsorbates. However, in order to calculate the hydrodynamic frictional coefficient, a cylindrical geometry must be assumed. Therefore, the effective anhydrous diameter of the SWNT−surfactant complex, Φ_a, is defined such that the actual volume of the discrete surfactant molecules on the surface of the SWNT is equal to the volume enclosed between the diameters Φ_a and Φ_{out}. The hydrodynamic diameter of the cylindrical SWNT−surfactant complexes, Φ'_a, is expected to be larger than Φ_a due to viscous frictional effects resulting from strongly bound water molecules in the first hydration layer. Fontell[45,46] has characterized the first hydration layer in sodium cholate micelles in water and has determined that 20 water molecules per surfactant molecule contribute to hydrodynamic friction. A significantly larger hydration layer must be accounted for when calculating the buoyant density of surfactant−SWNT complexes. The extent of the fully hydrated diameter, Φ_h, can be determined from the measured buoyant density, ρ_b. All hydration layers are assumed to have a density of 1.0 g cm^{-3}.

To determine L, X, V', Φ'_a, and Φ_a, multiple relations are constructed. First, the Broersma relationship for rigid rods is considered

$$f = \frac{3\pi\eta_o L}{\ln\left(\frac{L}{\Phi' a}\right) + E} \tag{7}$$

where E accounts for end effects.[34−37] Second, Φ'_a is related to Φ_a by a geometrical relationship, taking into account the hydration layer measured by Fontell, such that

$$\pi\left[\left(\frac{\Phi' a}{2}\right)^2 - \left(\frac{\Phi_a}{2}\right)^2\right] = \frac{X \times 20\frac{\text{mol}}{\text{mol}}}{N_A} \times 1.0\text{cm}^3\ \text{g}^{-1} \tag{8}$$

Next, the anhydrous molecular weight of the sodium cholate−SWNT complex, M, is decomposed into two components: the molecular weight of the adsorbed surfactant per nanotube, M_{SC}, and the molecular weight of the nanotube, M_{NT}, such that

$$M = M_{SC} + M_{NT} \tag{9a}$$

$$M_{SC} = X \times L \times \text{MW}_{SC} \tag{9b}$$

$$M_{NT} = \rho_g \times L \times \pi \times \Phi_{NT} \tag{9c}$$

where the sheet density of graphene, ρ_g, is 458.3 Da nm^{-2}, and the molecular weight of sodium cholate molecule, MW_{SC}, is 430.55 g mol^{-1}. Finally, the anhydrous volume of the sodium cholate−SWNT complex, υM, is related to the volume of the adsorbed surfactant molecules per nanotube, V_{SC}, and the volume of the nanotube, V_{NT}, such that

$$\upsilon M = V_{SC} + V_{NT} \tag{10a}$$

$$V_{SC} = V' \times X \times L \tag{10b}$$

$$V_{NT} = \pi\left[\left(\frac{\Phi_{out}}{2}\right)^2 - \left(\frac{\Phi_{in}}{2}\right)^2\right]L \tag{10c}$$

The results from the analysis of the structure of sodium cholate−SWNT complexes are listed in Table I. The mode anhydrous molar mass, M, of the surfactant−SWNT complex is 750 000 ± 340 000 Da. The surfactant loading ratio is 1.5 ± 0.3 g surfactant/g nanotube. Thus, 60% of the molecular weight of the complex results from the surfactant. A similar surfactant loading ratio of 1.5 g/g was previously determined by Grossiord *et al.* for sodium dodecyl sulfate encapsulated SWNTs *via* thermogravimetric analysis.[47] The mode length, L, of the sample of SWNTs is 290 ± 190 nm, which falls within the range of lengths measured for CoMoCAT-grown SWNTs isolated by DGU[2] (100−500 nm). The linear density of adsorbed surfactant along the length of the SWNT, X, is 3.6 ± 0.8 nm^{-1}.

A (6,5) SWNT encapsulated by sodium cholate with the aforementioned parameters is depicted in Figure 6. Even though the orientation and molecular spacings have been arbitrarily defined, the figure demonstrates that a considerable portion of the nanotube surface remains bare at a linear density of 3.6 nm^{-1}. The linear packing density of sodium cholate on the surface of a SWNT can be compared to the packing density of sodium cholate on graphene. Sasaki *et al.* report a packing density of 0.38 sodium cholate molecules per nm^2 of graphene at 25 °C.[48] The corresponding sheet packing densities for sodium cholate adsorbed to SWNTs are 0.97 ± 0.23 and 0.65 ± 0.14 nm^{-2} evaluated at Φ_{out} = 1.09 nm and Φ_a = 1.77 nm, respectively. The static surface area (evaluated at Φ_{out} = 1.09 nm) occupied by

TABLE I. Constant and Fit Parameters for Sodium Cholate Encapsulated (6,5) SWNTs

parameter	description	value[a]
υ	anhydrous partial specific volume	0.53 ± 0.03 cm^3 g^{-1}
M	anhydrous molar mass	750000 ± 340000 Da
s	sedimentation coefficient at experimental conditions	9.9 ± 0.1 Sv
s (corrected)	corrected sedimentation coefficient[b]	10.4 ± 0.1 Sv
D	diffusion coefficient at experimental conditions	7 ± 2 μm^2 s^{-1}
D (corrected)	corrected diffusion coefficient[b]	7 ± 2 μm^2 s^{-1}
f	hydrodynamic frictional coefficient at experimental conditions	$(5.8 \pm 2.6) \times 10^{-10}$ N s m^{-1}
f (corrected)	corrected hydrodynamic frictional coefficient[b]	$(5.5 \pm 2.5) \times 10^{-10}$ N s m^{-1}
Φ_{NT}	core diameter of a bare (6, 5) SWNT	0.75 nm
Φ_A	anhydrous diameter	1.8 ± 0.15 nm
Φ_H	fully hydrated diameter	5.5 ± 0.28 nm
L	length of the SWNT	290 ± 190 nm
X	number of sodium cholate molecules adsorbed per length of SWNT	3.6 ± 0.8 nm^{-1}
V'	molar volume of a sodium cholate molecule adsorbed to the surface of a SWNT	270 ± 20 cm^3 mol^{-1}

[a]Values without errors are constants. Values with errors were determined by fitting of the experimental data. [b]Corrected data are adjusted for a standardized temperature, solvent density, and viscosity of 20 °C, 0.9982 g cm^{-3}, and 1.002 centipoise, respectively. Experimental conditions were 22 °C, 1.0027 g cm^{-3}, and 1.053 centipoise, respectively.

one sodium cholate molecule absorbed to a SWNT surface is 70 Å^2. Accordingly, 72 ± 16% of the SWNT surface is occupied. In comparison, 26% of the graphene surface is occupied at a packing density of 0.38 sodium cholate molecules per nm^2 of graphene. Thus, the sheet packing density of sodium cholate on SWNTs significantly exceeds that measured on graphene.

The molar volume of sodium cholate on the surface of the SWNT, V', is 270 ± 20 cm^3 mol^{-1}, which is comparable to the theoretically calculated van der Waals volume[49] of 245 cm^3 mol^{-1}, the theoretically calculated Connolly volume of 267 cm^3 mol^{-1}, and the experimentally measured[45,46] molar volume of 320 cm^3 mol^{-1} in a micelle. The similarity of V' to the theoretically calculated Connolly volume implies an efficient placement of the surfactant molecules on the surfaces of the SWNTs such that there is little solvent-inaccessible empty space between the sodium cholate molecules and the SWNT surface or between neighboring sodium cholate molecules (Figure 6).

In the Supporting Information, three additional samples of DGU sorted sodium cholate encapsulated SWNTs that were collected from denser bands in the same density gradient[1] are analyzed. Similar $\alpha(s)$ distributions are determined that are shifted to higher sedimentation coefficients by 1−2 Sv (Figure S1 and Table SI in the Supporting Information). These shifts are compared with scaling predictions (Figure S2 in the Supporting Information) that explore the effects of nanotube diameter and length, surfactant packing density, and hydration on the sedimentation coefficient and buoyant density of surfactant encapsulated SWNTs. These scaling predictions are analyzed in order to gain insight into potential physical among the different sodium cholate−SWNT samples.

Effects of Aggregation. While O'Connell *et al.* were the first to demonstrate that isolated and aggregated single-walled carbon nanotubes (SWNTs) could be separated in an ultracentrifuge by exploiting differences in the rate of their centrifugal sedimentation,[12] the sedimentation coefficients of isolated and bundled SWNTs have not been experimentally quantified. In order to quantify the sedimentation of bundled SWNTs, a sample of sodium cholate encapsulated SWNTs containing a significant fraction of bundles was also studied using analytical ultracentrifugation. The sample

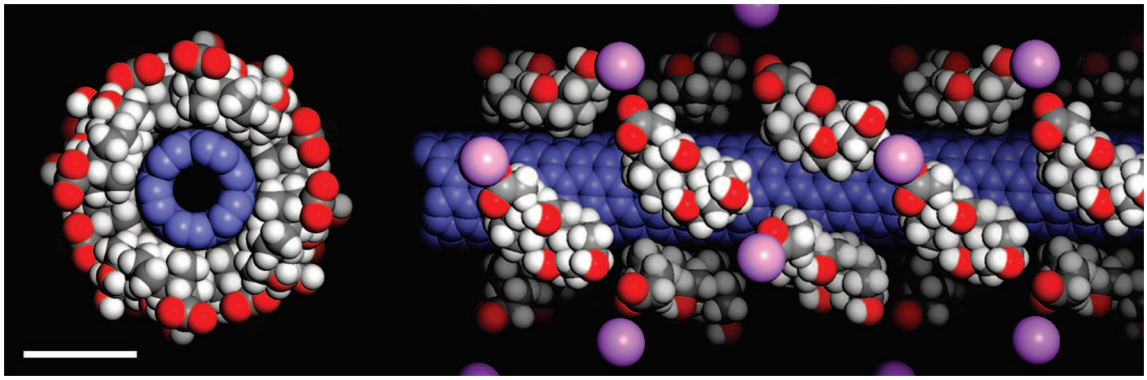

Figure 6. Schematic depicting the arrangement of sodium cholate around a (6,5) SWNT that matches the packing parameters determined in Table I. Purple, red, gray, blue, and white atoms represent Na^+, O, C (as part of sodium cholate), C (as part of nanotube), and H. The scale bar is 1 nm.

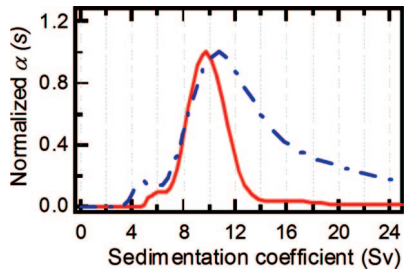

Figure 7. The α(*s*) distributions for sodium cholate encapsulated SWNTs sorted *via* DGU (red, solid) and not sorted by DGU (blue, dashed).

containing bundles was ultrasonicated, but the DGU process was not utilized to remove bundles. The regularized α(*s*) distribution for this partially bundled sample is plotted in Figure 7 in comparison with the α(*s*) distribution for DGU isolated SWNTs. Like the samples sorted by DGU, the α(*s*) distribution for the partially bundled sample has a maximum in the range of 10−12 Sv. However, unlike the sample sorted by DGU, the α(*s*) distribution for the partially bundled sample contains a long tail that extends past 100 Sv.

To better understand the sedimentation coefficient and buoyant density of bundled nanotubes, the following model was developed. The model assumes that all bundles are cylindrical and can be characterized by an outer diameter, Φ_{agg}. In the model, the two-dimensional packing density of adsorbed sodium cholate was kept constant at 1.0 molecules nm^{-2}, which is the packing density of sodium cholate on the surfaces of isolated SWNTs (evaluated at Φ_{out}) that was previously determined for isolated SWNTs. The molar volume of sodium cholate molecules on the surface of the bundles was assumed to be constant and equal to 270 cm^3 mol^{-1}. Furthermore, the effective thicknesses of the buoyancy hydration layer $1/2(\Phi_h - \Phi_a) = 1.9$ nm was kept constant, independent of the bundle size in the model. A van der Waals spacing of 0.35 nm was assumed between the walls of the SWNTs in the bundles, and the length of the bundles was held constant and equivalent to the mode length of the isolated SWNTs studied in the previous section (290 nm).

The results of the model are depicted in Figure 8. Substantial increases in the sedimentation coefficient of bundled SWNTs are observed with even small increases in Φ_{agg}. In the limit of large Φ_{agg}, *s* increases as $(\Phi_{agg})^2 \ln (L/\Phi_{agg})$. Thus, while an isolated SWNT will have a $s = 10$ Sv, a bundle of SWNTs of $\Phi_{agg} = 5$ nm will have a substantially larger $s = 100$ Sv.

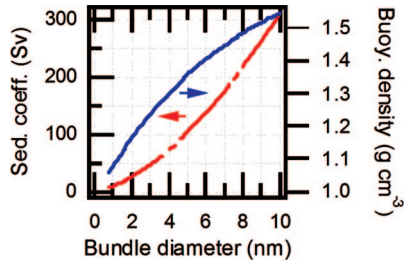

Figure 8. Calculated sedimentation coefficient (red, dashed) and buoyant density (blue, solid) of sodium cholate encapsulated SWNTs as a function of bundle diameter.

It can be concluded that the high-end tail in the α(*s*) distribution for sodium cholate encapsulated SWNTs not sorted by DGU (Figure 7) is due to the existence of bundles that are otherwise removed by DGU, and by comparing the α(*s*) distribution of isolated and bundled SWNTs, the effectiveness of the O'Connell method for separating isolated and bundled SWNTs can be analyzed. Specifically, it is observed that the long tail in the α(*s*) distribution for bundled SWNTs overlaps the peak in the α(*s*) distribution near 11 Sv that is attributed to isolated SWNTs (Figure 7). As a result of the overlap, the complete separation of isolated and bundled SWNTs by sedimentation-based centrifugation is unlikely.

Understanding this limitation is important when attempting to prepare solutions of unbundled, isolated SWNTs for fundamental studies and applications. In contrast with sedimentation-based separation techniques, DGU is likely a more sensitive means of sorting isolated and bundled SWNTs. This claim is supported by the α(*s*) distributions presented in Figure 7 and the findings of Crochet *et al.* who have observed exceptionally high fluorescence quantum yields from DGU-sorted semiconducting SWNTs.[5] Band gap fluorescence from semiconducting SWNTs is expected to be quenched even in small bundles of SWNTs due to the statistical likelihood of the presence of metallic SWNTs. Our study also points out the possible limitations of DGU for separating isolated and bundled SWNTs. In particular, the buoyant density of a small bundle of SWNTs can fall into the same range expected for isolated SWNTs, depending on the diameter of the SWNT and the packing density of surfactant on its surface (Figure 8). This limitation may be alleviated by utilizing different types of surfactants, thus manipulating the densities of surfactant−SWNT complexes.

CONCLUSIONS

In conclusion, the sedimentation and diffusion of nanotube−surfactant complexes have been studied using an analytical ultracentrifuge. The rate of sedimentation of single-walled carbon nanotubes (SWNTs) from the same source was found to vary significantly depending on the solvent and preprocessing procedures such as density gradient ultracentrifugation (DGU). Detailed analysis of a model fraction of sodium cholate encapsulated SWNTs sorted by diameter and buoyant density resulted in specific information regarding the structure of the surfactant−SWNT complexes. Specifically, the sodium cholate−SWNT complexes were found to have an anhydrous partial specific volume of 0.53 ± 0.03 cm^{-3} g and an adsorbed linear surfactant density of 3.6 ± 0.8 molecules nm^{-1}. Additionally, the

anhydrous molar volume of the surfactant molecules on the SWNT surface was 270 ± 20 cm^3 mol^{-1}. The technique of analytical ultracentrifugation should prove useful for analyzing surfactant−SWNT interactions for a variety of systems including electronic-type and chirality-specific interactions. Also, it is expected to impact the design of future centrifuge-based sedimentation and buoyancy-based SWNT experiments.

METHODS

Experimentally, an X-LA 70 (Beckman-Coulter) analytical ultracentrifuge was used to directly measure the redistribution of SWNTs in a centrifugal force field. This instrument enabled the characterization of the sedimentation and diffusion of SWNTs *in situ* at an angular velocity of 27 000 rotations per minute. Dispersed SWNTs and reference aqueous surfactant solutions were loaded into two-hole Epon cells equipped with quartz windows. These cells were housed in a four-cell rotor (Ti-60, Beckman-Coulter), which was kept at a constant temperature of 22 °C. The optical density of the SWNT solutions at 574 nm (at which there is negligible surfactant and solvent absorbance) was measured as a function of time and position to track the redistribution of the SWNTs as depicted in Figure 2, and experiments were typically continued for 1−2 h until predominantly all the SWNTs had sedimented to the bottom of the cells.

Raw SWNTs produced by the CoMoCAT method (Southwest Nanotechnologies, Inc.) were utilized in all instances. Sodium cholate (SC, 98%, Sigma-Aldrich) was utilized as an encapsulating agent for the dispersion of the SWNTs.[1,2,12,15,17] First, 1 mg/mL of as-grown SWNTs was added to aqueous solutions of 20 mg/mL of surfactant. Then, aggregations and bundles of SWNTs were disseminated using a horn ultrasonicator coupled to a tapered extension immersed in the solutions. Subsequently, the samples were centrifuged at 22 °C (TLA100.3 rotor, Beckman) at 124 000*g* for 14 min to remove grossly insoluble SWNT aggregates, catalysts, and contaminants, leaving isolated and small bundles of SWNTs in the supernatant, which was collected. At this stage, in some instances, the SWNT solutions were also sorted by diameter in density gradients according to previously published procedures.[1,2] After sorting in density gradients, these SWNTs were then dialyzed in surfactant solutions to remove residual density gradient media using 10K MWCO membranes (Pierce Biotechnology, Inc.). Some SWNT samples were also dialyzed in D_2O surfactant solutions in parallel for studies aimed at determining the anhydrous partial specific volume.

Acknowledgment. This work was supported by the Department of Energy under award number DE-FG02-00ER45810, the U.S. Army Telemedicine and Advanced Technology Research Center under award number DAMD17-05-1-0381, and the National Science Foundation under award numbers EEC-0647560 and DMR-0706067. A National Defense Science and Engineering Graduate Fellowship (M.S.A.), National Science Foundation Graduate Fellowship (M.S.A.), Alfred P. Sloan Research Fellowship (M.C.H.), and Northwestern University Undergraduate Research Grant (J.S.) are also gratefully acknowledged.

Supporting Information Available: Scaling predictions for how sedimentation coefficient and buoyant density should vary as a function of the nanotube diameter, surfactant concentration, and the extent of the hydration layer. This material is available free of charge *via* the Internet at http://pubs.acs.org.

REFERENCES AND NOTES

1. Arnold, M. S.; Green, A. A.; Hulvat, J. F.; Stupp, S. I.; Hersam, M. C. Sorting Carbon Nanotubes by Electronic Structure Using Density Differentiation. *Nat. Nanotechnol.* **2006**, *1*, 60–65.
2. Arnold, M. S.; Stupp, S. I.; Hersam, M. C. Enrichment of Single-Walled Carbon Nanotubes by Diameter in Density Gradients. *Nano Lett.* **2005**, *5*, 713–718.
3. Chen, Z. H.; Du, X.; Du, M. H.; Rancken, C. D.; Cheng, H. P.; Rinzler, A. G. Bulk Separative Enrichment in Metallic or Semiconducting Single-Walled Carbon Nanotubes. *Nano Lett.* **2003**, *3*, 1245–1249.
4. Crochet, J.; Clemens, M.; Hertel, T. Optical Properties of Structurally Sorted Single-Wall Carbon Nanotube Ensembles. *Phys. Status Solidi B* **2007**, *244*, 3964–3968.
5. Crochet, J.; Clemens, M.; Hertel, T. Quantum Yield Heterogeneities of Aqueous Single-Wall Carbon Nanotube Suspensions. *J. Am. Chem. Soc.* **2007**, *129*, 8058–8059.
6. Green, A. A.; Hersam, M. C. Ultracentrifugation of Single-Walled Nanotubes. *Mater. Today* **2007**, *10*, 59–60.
7. Hennrich, F.; Arnold, K.; Lebedkin, S.; Quintilla, A.; Wenzel, W.; Kappes, M. M. Diameter Sorting of Carbon Nanotubes by Gradient Centrifugation: Role of Endohedral Water. *Phys. Status Solidi B* **2007**, *244*, 3896–3900.
8. Hertel, T.; Zhu, Z. P.; Crochet, J.; McPheeters, C.; Ulbricht, H.; Resasco, D. Exciton Dynamics Probed in Carbon Nanotube Suspensions with Narrow Diameter Distribution. *Phys. Status Solidi B* **2006**, *243*, 3186–3191.
9. Jones, M.; Engtrakul, C.; Metzger, W. K.; Ellingson, R. J.; Nozik, A. J.; Heben, M. J.; Rumbles, G. Analysis of Photoluminescence from Solubilized Single-Walled Carbon Nanotubes. *Phys. Rev. B* **2005**, *71*, 115426.
10. Matarredona, O.; Rhoads, H.; Li, Z. R.; Harwell, J. H.; Balzano, L.; Resasco, D. E. Dispersion of Single-Walled Carbon Nanotubes in Aqueous Solutions of the Anionic Surfactant NaDDBS. *J. Phys. Chem. B* **2003**, *107*, 13357–13367.
11. Nair, N.; Kim, W. J.; Braatz, R. D.; Strano, M. S. Dynamics of Surfactant-Suspended Single-Walled Carbon Nanotubes in a Centrifugal Field. *Langmuir* **2008**, *24*, 1790–1795.
12. O'Connell, M. J.; Bachilo, S. M.; Huffman, C. B.; Moore, V. C.; Strano, M. S.; Haroz, E. H.; Rialon, K. L.; Boul, P. J.; Noon, W. H.; Kittrell, C.; et al. , Band Gap Fluorescence from Individual Single-Walled Carbon Nanotubes. *Science* **2002**, *297*, 593–596.
13. Strano, M. S.; Moore, V. C.; Miller, M. K.; Allen, M. J.; Haroz, E. H.; Kittrell, C.; Hauge, R. H.; Smalley, R. E. The Role of Surfactant Adsorption During Ultrasonication in the Dispersion of Single-Walled Carbon Nanotubes. *J. Nanosci. Nanotechnol.* **2003**, *3*, 81–86.
14. Wei, L.; Wang, B.; Goh, T. H.; Li, L. J.; Yang, Y. H.; Chan-Park, M. B.; Chen, Y. Selective Enrichment of (6,5) and (8,3) Single-Walled Carbon Nanotubes *via* Cosurfactant Extraction from Narrow (n,m) Distribution Samples. *J. Phys. Chem. B* **2008**, *112*, 2771–2774.
15. Wenseleers, W.; Vlasov, I. I.; Goovaerts, E.; Obraztsova, E. D.; Lobach, A. S.; Bouwen, A. Efficient Isolation and Solubilization of Pristine Single-Walled Nanotubes in Bile Salt Micelles. *Adv. Funct. Mater.* **2004**, *14*, 1105–1112.
16. Yu, A. P.; Bekyarova, E.; Itkis, M. E.; Fakhrutdinov, D.; Webster, R.; Haddon, R. C. Application of Centrifugation to the Large-Scale Purification of Electric Arc-Produced Single-Walled Carbon Nanotubes. *J. Am. Chem. Soc.* **2006**, *128*, 9902–9908.
17. Zheng, M.; Jagota, A.; Semke, E. D.; Diner, B. A.; McLean, R. S.; Lustig, S. R.; Richardson, R. E.; Tassi, N. G. DNA-Assisted Dispersion and Separation of Carbon Nanotubes. *Nat. Mater.* **2003**, *2*, 338–342.
18. Hersam, M. C. Progress towards Monodisperse Single-Walled Carbon Nanotubes. *Nat. Nanotechnol.* **2008**, *3*, 387–394.
19. Baughman, R. H.; Zakhidov, A. A.; de Heer, W. A. Carbon Nanotubes—The Route toward Applications. *Science* **2002**, *297*, 787–792.
20. Charlier, J. C.; Issi, J. P. Electronic Structure and Quantum Transport in Carbon Nanotubes. *Appl. Phys. A* **1998**, *67*, 79–87.

21. Ostojic, G. N.; Zaric, S.; Kono, J.; Strano, M. S.; Moore, V. C.; Hauge, R. H.; Smalley, R. E. Interband Recombination Dynamics in Resonantly Excited Single-Walled Carbon Nanotubes. *Phys. Rev. Lett.* **2004**, *92*, 117402-1–117402-4.
22. Kim, W. J.; Nair, N.; Lee, C. Y.; Strano, M. S. Covalent Functionalization of Single-Walled Carbon Nanotubes Alters Their Densities Allowing Electronic and Other Types of Separation. *J. Phys. Chem. C* **2008**, *112*, 7326–7331.
23. Lu, Q.; Keskar, G.; Ciocan, R.; Rao, R.; Mathur, R. B.; Rao, A. M.; Larcom, L. L. Determination of Carbon Nanotube Density by Gradient Sedimentation. *J. Phys. Chem. B* **2006**, *110*, 24371–24376.
24. Green, A. A.; Hersam, M. C. Colored Semitransparent Conductive Coatings Consisting of Monodisperse Metallic Single-Walled Carbon Nanotubes. *Nano Lett.* **2008**, *8*, 1415–1422.
25. Miyata, Y.; Yanagi, K.; Maniwa, Y.; Kataura, H. Highly Stabilized Conductivity of Metallic Single Wall Carbon Nanotube Thin Films. *J. Phys. Chem. C* **2008**, *112*, 3591–3596.
26. Kiowski, O.; Arnold, K.; Lebedkin, S.; Hennrich, F.; Kappes, M. M. Direct Observation of Deep Excitonic States in the Photoluminescence Spectra of Single-Walled Carbon Nanotubes. *Phys. Rev. Lett.* **2007**, *99*, 237402-1–237402-4.
27. Zhu, Z. P.; Crochet, J.; Arnold, M. S.; Hersam, M. C.; Ulbricht, H.; Resasco, D.; Hertel, T. Pump-Probe Spectroscopy of Exciton Dynamics in (6,5) Carbon Nanotubes. *J. Phys. Chem. C* **2007**, *111*, 3831–3835.
28. Qian, H.; Georgi, C.; erson, N.; Green, A. A.; Hersam, M. C.; Novotny, L.; Hartschuh, A. Exciton Energy Transfer in Pairs of Single-Walled Carbon Nanotubes. *Nano Lett.* **2008**, *8*, 1363–1367.
29. Maeda, Y.; Kimura, S.; Kanda, M.; Hirashima, Y.; Hasegawa, T.; Wakahara, T.; Lian, Y. F.; Nakahodo, T.; Tsuchiya, T.; Akasaka, T.; et al. , Large-Scale Separation of Metallic and Semiconducting Single-Walled Carbon Nanotubes. *J. Am. Chem. Soc.* **2005**, *127*, 10287–10290.
30. Halle, B.; Davidovic, M. Biomolecular Hydration: From Water Dynamics to Hydrodynamics. *Proc. Natl. Acad. Sci. U.S.A.* **2003**, *100*, 12135–12140.
31. Hearst, J. E.; Vinograd, J. Net Hydration of Deoxyribonucleic Acid. *Proc. Natl. Acad. Sci. U.S.A.* **1961**, *47*, 825–830.
32. Hearst, J. E.; Vinograd, J. A 3-Component Theory of Sedimentation Equilibrium in a Density Gradient. *Proc. Natl. Acad. Sci. U.S.A.* **1961**, *47*, 999–1004.
33. Schuck, P. Size-Distribution Analysis of Macromolecules by Sedimentation Velocity Ultracentrifugation and Lamm Equation Modeling. *Biophys. J.* **2000**, *78*, 1606–1619.
34. Broersma, S. Viscous Force and Torque Constants for a Cylinder. *J. Chem. Phys.* **1981**, *74*, 6989–6990.
35. Broersma, S. Viscous Force Constant for a Closed Cylinder. *J. Chem. Phys.* **1960**, *32*, 1632–1635.
36. Broersma, S. Rotational Diffusion Constant of a Cylindrical Particle. *J. Chem. Phys.* **1960**, *32*, 1626–1631.
37. Tirado, M. M.; Martinez, C. L.; Delatorre, J. G. Comparison of Theories for the Translational and Rotational Diffusion-Coefficients of Rod-Like Macromolecules—Application to Short DNA Fragments. *J. Chem. Phys.* **1984**, *81*, 2047–2052.
38. Duggal, R.; Pasquali, M. Dynamics of Individual Single-Walled Carbon Nanotubes in Water by Real-Time Visualization. *Phys. Rev. Lett.* **2006**, *96*, 246104.
39. Salvetat, J. P.; Briggs, G. A. D.; Bonard, J. M.; Bacsa, R. R.; Kulik, A. J.; Stockli, T.; Burnham, N. A.; Forro, L. Elastic and Shear Moduli of Single-Walled Carbon Nanotube Ropes. *Phys. Rev. Lett.* **1999**, *82*, 944–947.
40. Yakobson, B. I.; Couchman, L. S. *Dekker Encyclopedia of Nanoscience and Nanotechnology*; Marcel Dekker: New York, 2004; p 587.
41. Schuck, P. SEDFIT, version 10.09b; National Institutes of Health: 2007.
42. Tsyboulski, D. A.; Bachilo, S. M.; Weisman, R. B. Versatile Visualization of Individual Single-Walled Carbon Nanotubes with Near-Infrared Fluorescence Microscopy. *Nano Lett.* **2005**, *5*, 975–979.
43. Lu, Q.; Freedman, K. O.; Rao, R.; Huang, G.; Lee, J.; Larcom, L. L.; Rao, A. M.; Ke, P. C. Diffusion of Carbon Nanotubes with Single-Molecule Fluorescence Microscopy. *J. Appl. Phys.* **2004**, *96*, 6772–6775.
44. Kumar, K. N.; Eggeman, K. T.; Adams, J. L.; Michaelis, E. K. Hydrodynamic Properties of the Purified Glutamate-Binding Protein Subunit of the N-Methyl-D-Aspartate Receptor. *J. Biol. Chem.* **1991**, *266*, 14947–14952.
45. Fontell, K. Micellar Behaviour in Solutions of Bile-Acid Salts 0.3. Viscosity and Density Measurements in Aqueous Solutions. *Koll. Z. Z. Polym.* **1971**, *246*, 614–625.
46. Fontell, K. Micellar Behaviour in Solutions of Bile-Acid Salts 0.4. X-ray Study of Aqueous Solutions. *Koll. Z. Z. Polym.* **1971**, *246*, 710–718.
47. Grossiord, N.; van der Schoot, P.; Meuldijk, J.; Koning, C. E. Determination of the Surface Coverage of Exfoliated Carbon Nanotubes by Surfactant Molecules in Aqueous Solution. *Langmuir* **2007**, *23*, 3646–3653.
48. Sasaki, Y.; Nagata, H. D.; Fujii, Y. K.; Lee, S.; Nagadome, S.; Sugihara, G. A Thermodynamic Study on the Adsorption Behavior of Four Bile Salt Species on Graphite in Water. *Colloids Surf. B* **1997**, *9*, 169–176.
49. The van der Waals and Connolly molar volumes for sodium cholate were calculated using Materials Studio 4.1 (Accelrys, Inc.; San Diego, CA). The molecular structure of sodium cholate was derived from that of cholic acid which was determined from the Protein Data Bank (www.rcsb.org). A probe radius of 1.4 Å (corresponding to the size of a water molecule) was utilized to calculate the Connolly molar volume.